

# Magnetic Guidance of Cochlear Implants: Proof-of-Concept and Initial Feasibility Study

James R. Clark

e-mail: james.r.clark@utah.edu

Lisandro Leon<sup>1</sup>

e-mail: l.leon@utah.edu

Department of Mechanical Engineering,  
University of Utah,  
Salt Lake City, UT 84112

Frank M. Warren

Department of Otolaryngology,  
Division of Otolology and Skull Base Surgery,  
Oregon Health & Science University,  
Portland, OR 97239  
e-mail: warrenf@ohsu.edu

Jake J. Abbott

Department of Mechanical Engineering,  
University of Utah,  
Salt Lake City, UT 84112  
e-mail: jake.abbott@utah.edu

*Cochlear implants have become a standard treatment for many with severe to profound sensorineural hearing loss. However, delicate cochlear structures can be damaged during surgical insertion, which can lead to loss of residual hearing and decreased implant effectiveness. We propose a magnetic guidance concept in which a magnetically tipped cochlear implant is guided as it is inserted into the cochlea. In a scaled in vitro experimental study, we record insertion forces for nonguided and magnetically guided insertion experiments and compare the results. Results indicate that magnetic guidance reduced insertion forces by approximately 50%. Using first principles, we discuss the effects of scaling down our in vitro experiments, and account for realistic clinical dimensions. We conclude that scale-down effects are negligible, but to produce the same field strength as in our experiments and provide sufficient clearance between the patient and the manipulator, the magnet dimensions should be increased by approximately four times. [DOI: 10.1115/1.4007099]*

## 1 Introduction

A cochlear implant (CI) is an array of electrodes embedded in silicone that is surgically inserted into the scala tympani (ST) chamber of the cochlea to electrically stimulate the nerves responsible for hearing (Fig. 1). Cochlear implants have become a standard treatment for many with severe to profound sensorineural hearing loss. However, the majority of CI users still have difficulty understanding speech in an environment with competing noise and difficulty distinguishing a full range of sounds. Future CIs will need to address three widely accepted goals [1]: (1) deeper insertion into the ST to access lower frequency cochlear neurons, (2) better proximity to the modiolus (the central axis of the cochlea) for greater operating efficiency, defined as a reduc-

tion in the stimulus charge required to produce a comfortable loudness level, and (3) reduced intracochlear damage during surgical insertion (Fig. 2) to preserve residual hearing and improve implant effectiveness.

Two major factors that contribute to the extent of damage during insertion are electrode-array design and surgical technique [2]. Numerous electrode-array designs have been developed with varied success [1–5], and to date, no single design has been able to achieve all three objectives of deeper insertion, proximity to the modiolus, and consistent atraumatic insertion [1]. Straight free-fitting CIs designed for deeper insertions can increase the risk of trauma and typically do not lie close to the modiolus [3,4]. Pre-curved CIs with stylets, designed to hug the modiolus, can be inserted with minimal insertion forces for nearly the entire procedure using the advance-off-stylet technique [6–8]. However, advancing the CI off the stylet too early can cause the implant tip to fold-over, and late stylet removal can result in the implant contacting the ST outer wall, potentially causing damage. The variability in human cochlear dimensions poses a challenge when using stylet withdrawal techniques, since the point during insertion when stylet removal should begin is patient dependent [1]. Further, insertions into the apical regions of the cochlea are not possible with these designs because they are significantly shorter than those designed for deep insertions.

Due to the limitations of existing CIs, several groups have developed electrode-array prototypes to achieve a modiolus-hugging position within the cochlea [9], with some actively bent or steered during insertion to minimize insertion trauma [10–13], though only Ref. [13] demonstrated insertion force reduction in their publication. Some designs [10,12,13] use mechanical means built into the CI to achieve bending, which can increase the stiffness of the CI as it is being inserted. If the CI is not formed to fit the ST well, or is misdirected down the channel, the increased CI stiffness could result in increased intracochlear trauma. Some are not reversible [9,12] or require sufficient perilymph fluid to actuate [9,11], which may be problematic if, during surgery, reinsertion is necessary [2] or sufficient fluid is lost. Finally, the wide variability in surgical force application has motivated the use of robotic assistance [14–16] and optimized path planning [13] to produce more repeatable insertions.

In this paper, we propose a magnetic guidance concept in which a magnetically tipped CI is guided as it is inserted into the cochlea. With a rotating manipulator magnet located near the patient's head, we apply magnetic torque to the implant tip, causing it to bend away from the ST walls during insertion. We conduct proof-of-concept experiments of two proposed magnetic guidance methods, using an automated experimental apparatus to

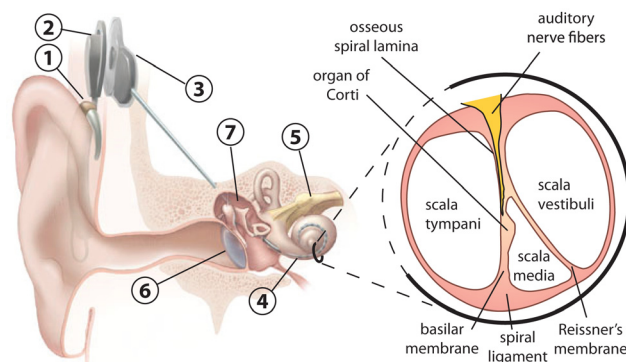


**Fig. 1 Cochlear implant system with blow-up of cochlea cross-section showing the location of several cochlear structures (National Institutes of Health public domain image with added labels). Labeled items are the (1) microphone and speech processor, (2) transmitter, (3) receiver, (4) electrode array inserted into the cochlea (referred to as the “cochlear implant” herein), (5) auditory nerve, (6) ear drum, and (7) ossicles.**

<sup>1</sup>Corresponding author.

Manuscript received July 29, 2011; final manuscript received April 3, 2012; published online August 10, 2012. Assoc. Editor: Foster B. Stulen.

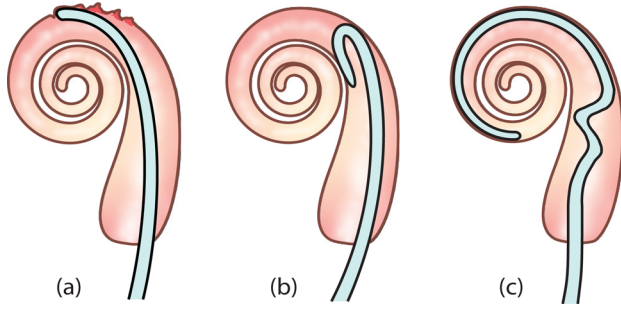


**Fig. 2** Some causes of intracochlear trauma during cochlear implant insertions: (a) tip scraping [4], (b) tip fold-over [1], and (c) buckling [2,4]

insert a scaled magnetically tipped implant prototype into a custom 3:1 scale ST phantom [17]. We record insertion forces during nonguided and magnetically guided insertion experiments and compare the results. The data show that magnetic guidance can reduce insertion forces by approximately 50%. Our method is consistent with the current practice of using insertion force measurements (which encode implant–ST contact forces) as a metric for evaluation of insertion trauma [6–8,13–15]. Our approach is an adaptable means of guidance that could be robotically implemented as either a supervised automated process or a robotic system under surgeon manipulation. The basic idea of magnetic guidance for CIs has been proposed previously [18], but no technical results were presented to demonstrate how it could be accomplished in practice.

## 2 Magnetic Guidance Concept

A clinical concept for magnetically guided CI insertions is shown in Fig. 3. To achieve CI guidance, a small permanent magnet is located at the tip of the implant. A large manipulator magnet located near the patient’s head is used to apply a magnetic field to the CI tip. The manipulator magnet’s orientation is controlled by a motor, with the magnet’s magnetization direction perpendicular to the axis of rotation. The rotation axis is approximately aligned with the central spiral axis of the cochlea. As the CI is inserted, the manipulator magnet is rotated to actively bend the implant, directing it away from cochlear walls and reducing the contact forces between the CI and the walls of the ST. The motor is allowed to translate along its rotation axis, varying the distance

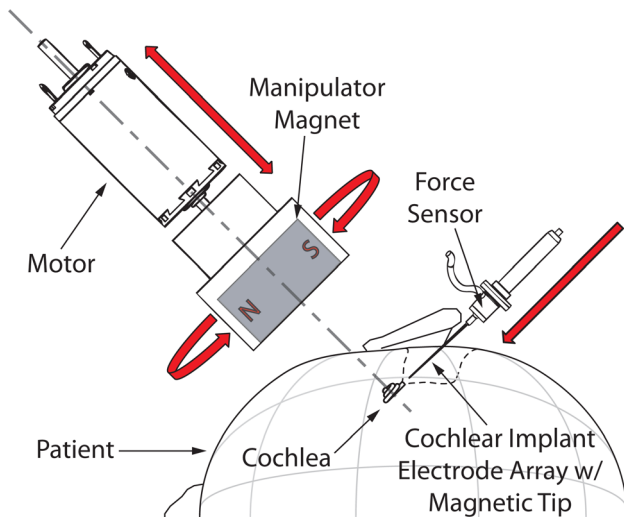


**Fig. 3** Concept for magnetically guided cochlear implant surgery. Red wide arrows indicate the three controlled degrees of freedom.

between the manipulator magnet and the patient, effectively changing the strength of the applied magnetic field acting on the CI tip. The CI insertion is automated and synchronized with the movement of the manipulator magnet in our developed control software.

The field  $\mathbf{B}$  (T) generated by the manipulator magnet, modeled as a magnetic dipole  $\mathbf{M}$  ( $\text{A} \cdot \text{m}^2$ ), can be approximated by the point–dipole model

$$\mathbf{B}(\mathbf{p}) = \frac{\mu_0}{4\pi|\mathbf{p}|^3} \left( \frac{3(\mathbf{M} \cdot \mathbf{p})\mathbf{p}}{|\mathbf{p}|^2} - \mathbf{M} \right) \quad (1)$$

where  $\mu_0$  is the permeability of free space ( $\mu_0 = 4\pi \times 10^{-7} \text{ T} \cdot \text{m} \cdot \text{A}^{-1}$ ) and  $\mathbf{p}$  is the location of a point in space with respect to the magnet’s center ( $\text{m}$ ). A magnet’s dipole strength  $|\mathbf{M}|$  is the product of its volume ( $\text{m}^3$ ) and its average magnetization ( $\text{A}/\text{m}$ ). Magnetic forces and torques will act upon any magnet placed within this nonuniform field. If we represent the permanent magnet embedded in the CI’s tip by the dipole  $\mathbf{m}$ , then the force and torque acting on it due to the manipulator magnet are

$$\mathbf{F} = \left[ \frac{\partial}{\partial x} \mathbf{B} \quad \frac{\partial}{\partial y} \mathbf{B} \quad \frac{\partial}{\partial z} \mathbf{B} \right]^T \mathbf{m} \quad (2)$$

$$\mathbf{T} = \mathbf{m} \times \mathbf{B} \quad (3)$$

where  $\mathbf{B}$  is the field at the location of  $\mathbf{m}$ ,  $\mathbf{F}$  is force (N), and  $\mathbf{T}$  is the torque (N·m), expressed in the same frame in which the spatial derivatives are taken [19]. From Eq. (2) we see that the force in a given direction is the inner product of the derivative of the field in that direction and the magnetization of the magnet placed in the field. This means that a force will only act on the magnet in a given direction if both a field gradient and some component of  $\mathbf{m}$  exist in that direction. The applied torque is the cross product of the magnet’s dipole with the applied field, meaning that a torque will only act on the magnet if its dipole is not parallel to the applied field.

Figure 4 demonstrates how our clinical configuration allows Eqs. (1)–(3) to be simplified. Note the CI magnet is positioned approximately on the manipulator magnet’s rotation axis and can be rotated about the  $y$ -axis in the  $xz$ -plane to any rotation angle  $\theta$  between  $\mathbf{m}$  and the local  $\mathbf{B}$ . The vector  $\mathbf{p}$  points from the manipulator magnet to the CI magnet. Moving the manipulator toward or away from the patient along the manipulator’s rotation axis will change the strength of the field applied at the CI tip, but the field direction will not change unless the manipulator magnet is rotated. Since CI tip rotations are largely confined to the  $xz$ -plane within the ST channel, the torque of Eq. (3) simplifies to

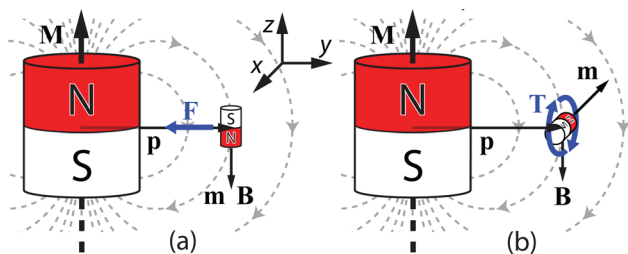


**Fig. 4** Magnetic force and torque in clinical arrangement of Fig. 3. The large magnet is the manipulator magnet, with the coordinate frame origin at its dipole center (shown offset for clarity). The implant tip magnet is placed along the manipulator’s rotation axis making  $\mathbf{M}$  and  $\mathbf{p}$  orthogonal. Two directions of the implant tip magnet with resulting forces and torques are shown. (a) Negative  $z$ -direction ( $\theta = 0$  deg): force in negative  $y$ -direction. (b) Negative  $x$ -direction ( $\theta = 90$  deg): negative torque about  $y$ -axis.

$$|\mathbf{T}| = |\mathbf{m}||\mathbf{B}|\sin(\theta) \quad (4)$$

Maximum torque occurs when the dipoles are perpendicular to one another; when the dipoles are aligned, the torque is zero. The general equation for the field strength in Eq. (1) and its gradient also simplify along the axis of the motor:

$$|\mathbf{B}| = \frac{\mu_0 |\mathbf{M}|}{4\pi |\mathbf{p}|^3} \quad (5)$$

$$\frac{d|\mathbf{B}|}{d|\mathbf{p}|} = -\frac{3\mu_0 |\mathbf{M}|}{4\pi |\mathbf{p}|^4} \quad (6)$$

Furthermore, after some manipulation, the magnetic force of Eq. (2) can be expressed in a form that more clearly shows its behavior when  $\mathbf{m}$  is located along the rotation axis:

$$\mathbf{F} = \frac{d|\mathbf{B}|}{d|\mathbf{p}|} \begin{bmatrix} 0 & 0 & 0 \\ 0 & 0 & -1 \\ 0 & -1 & 0 \end{bmatrix} \mathbf{m} \quad (7)$$

We see from Eq. (7) that no gradient exists in the x-direction (first row), whereas gradients do exist in the y- and z-directions (second and third rows, respectively). Since there is no x-direction gradient, forces will not act on the magnet in the x-direction for any  $\mathbf{m}$ . The second row indicates that a force will only act in the y-direction if some component of  $\mathbf{m}$  points in the z-direction. This force reaches a maximum magnitude when  $\mathbf{m}$  is completely aligned with the z-direction, as shown in Fig. 4(a). The third row indicates that a force will only act in the z-direction if some component of  $\mathbf{m}$  points in the y-direction; however, since the CI tip is confined to rotate largely in the xz-plane, the components of  $\mathbf{m}$  point largely in the x- and z-direction. Thus, we assume that the z-direction force is negligible. In practice, the CI tip rotation will not be strictly confined to the xz-plane, but the minor deviations we expect should only result in minor forces and torques along directions not shown in Fig. 4.

We have devised two control algorithms to synchronize the motions of the manipulator magnet and the CI insertion (Fig. 5). The first is the maximum-field method, which places the manipulator magnet as close to the patient as is physically possible for the duration of the insertion. By minimizing the separation distance between the manipulator magnet and the implant magnet ( $|\mathbf{p}|$ ), the magnitude of the magnetic field is always at its maxi-

imum, Eq. (5). Since the CI tip is nearly aligned with the manipulator magnet for much of the insertion due to attractive forces, the implant can be directed through the ST by simply rotating the manipulator magnet. Unfortunately, these attractive forces direct the CI tip toward the delicate basilar membrane (see Fig. 1 and Fig. 4(a)). The primary benefit of this algorithm is reduced complexity, as it does not require the use of a controlled linear stage to vary the distance between the manipulator magnet and the patient. The second algorithm is the maximum-torque method, in which the applied field is always maintained approximately perpendicular to the CI tip, resulting in a pure magnetic torque with negligible attractive forces (see Fig. 4(b)). That is, at any given separation distance ( $|\mathbf{p}|$ ), the maximum torque that can be applied to the implant occurs when the magnet dipoles are orthogonal to each other, Eq. (4). Unlike the first method, this requires variable distance between the manipulator magnet and the patient in order to control the amount of torque applied onto the CI tip throughout the insertion (since increasing torque is required for deeper insertions).

### 3 Experimental Methods

To validate the basic magnetic-guidance method, we constructed an automated experimental apparatus shown in Fig. 6 consisting of a CI prototype, a force sensor, custom mounting fixtures, an ST phantom, linear stages, a manipulator magnet, a servo system (not labeled), and a standard personal computer (not shown).

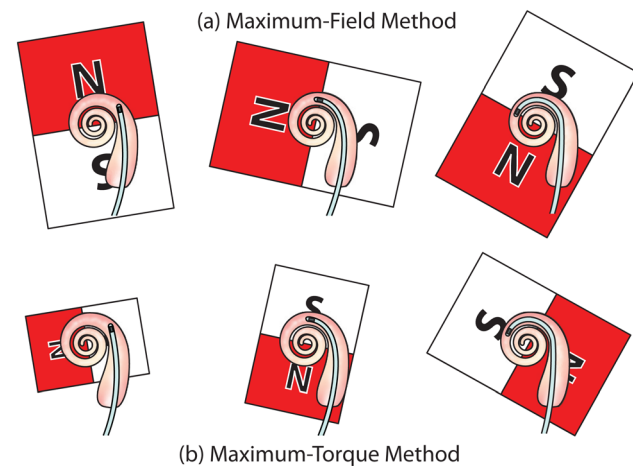


Fig. 5 Two guidance methods explored in experiments. (a) Maximum-field method: the dipoles are nearly aligned. (b) Maximum-torque method: the dipoles are nearly perpendicular. The increasing manipulator magnet size in the maximum-torque diagram indicates that the manipulator is advancing toward the cochlea.

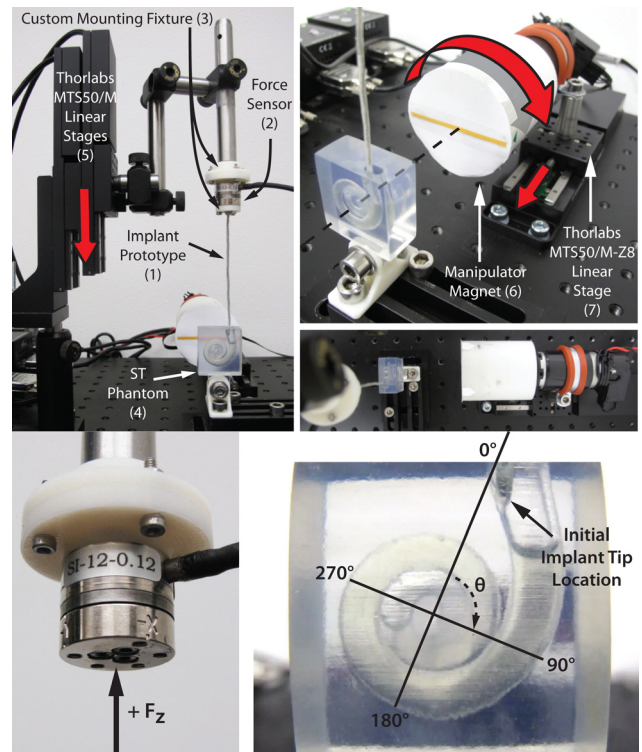


Fig. 6 Experimental setup. (top) The prototype (1) was attached to a force/torque sensor (2) with custom mounting fixtures (3) and inserted into a phantom (4) using linear stages (5). The manipulator (6) is attached to a brushed dc motor shaft and mounted to a linear stage (7), which translates the manipulator toward the phantom. The dashed line shows that the manipulator rotation axis and cochlear central spiral axis are aligned. The curved arrow above the manipulator (6) shows the manipulator rotation direction. The straight arrows on (5) and (7) show the translation direction of the linear stages. The stripe on the front of the manipulator marks the dipole direction of the enclosed axially magnetized magnet. (bottom-left) ATI Nano17 force/torque sensor with definition of positive force. (bottom-right) Insertion angle based on the phantom model [17].



**Fig. 7 (top)** The MED-EL practice electrode shown is a straight, free-fitting electrode array with a length of 32 mm, and it tapers from a base diameter of 1.3 mm to a tip diameter of 0.5 mm. **(bottom)** Our 3:1 prototype has a length of 83 mm and a constant diameter of 1.6 mm.

We constructed a prototype CI with a small (1 mm diameter  $\times$  2 mm long) permanent magnet (of approximate dipole strength  $2 \text{ mA}\cdot\text{m}^2$ ) embedded in its tip; the prototype is a 3:1 scale model of a free-fitting straight CI. Our goal was not to duplicate a scaled version of a commercial CI but to develop one that could be used to validate our magnetic guidance concept. We also wanted the prototype to qualitatively mimic some important properties of a real CI (such as the MED-EL practice electrode in Fig. 7), including graded stiffness, bending properties, and the use of silicone rubber. The process to fabricate the prototypes is shown in Fig. 8.

We inserted the implant into a custom 3:1 scale scala-tympani phantom filled with soap solution; the phantom's model, described in detail in Ref. [17], is based on published anatomical data and can be manufactured to a desired scale.

An ATI Nano17 six-axis force/torque sensor was used to collect force data during insertion experiments. Along the sensor z-axis, the minimum resolution is 3.125 mN and the maximum measurement uncertainty is 170 mN, which is the maximum amount of error in any single measurement. However, under certain loading conditions, the sensor performs significantly better. In the accompanying calibration report, measurement uncertainty of 1.7–3.4 mN was reported for sensor loading along its z-axis exclusively, which is the loading condition of our experimental setup.

Custom mounting fixtures, printed in ABSplus thermoplastic using a Dimension 3D printer, were used to attach the force sensor to the Thorlabs mounting posts and the implant prototype to the front (tool side) of the sensor.

The manipulator consists of a Delrin housing attached to a motor shaft with a 25.4-mm-diameter  $\times$  25.4-mm-long NdFeB permanent magnet placed in the housing. The cylindrical magnet is axially magnetized with a measured dipole strength of  $10.2 \text{ A}\cdot\text{m}^2$ .

The rotation of the manipulator magnet was controlled using commercial servo components, including a digital servo drive (Advanced Motion Controls DigiFlex Performance DPR Series), dc power supply (GW Instek GPS-3303), and a brushed dc motor and encoder unit (Maxon A-max 32 and HEDS 5540). The motion of the CI was captured through the transparent phantom using a commercial camera (Canon PowerShot G10). System control and data logging were performed with a personal computer running Windows.

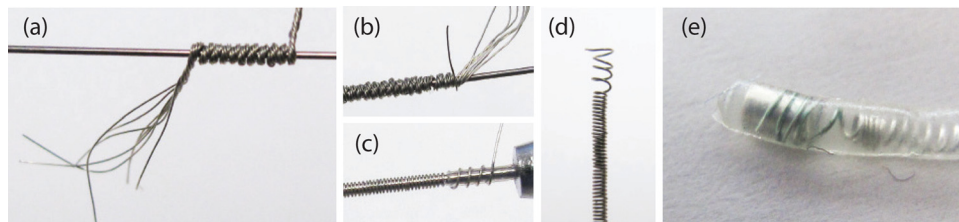


**Fig. 8** Key steps for production of the wire core used in the implant prototype. **(a)** Wires twisted together and wrapped around a cylindrical shaft. **(b)** Snip off one wire at a certain length and wrap the remaining wires. Repeat this process until only one wire is left. This creates a tapered stiffness, which was observed in the MED-EL device. **(c)** Wrap remaining wire around tubing to create a coil that the magnet can be slid into. **(d)** The result of the wire wrapping prior to placing the magnet. **(e)** Magnet is placed at the end of the coil and encased in silicone using an acrylic mold.

The experiments were conducted on a Thorlabs metric optical table with the following arrangement. The implant prototype was mounted to the vertically stacked stages oriented so that the prototype pointed downward. The 3:1 ST phantom was attached vertically to the table so that the entrance of the chamber was facing upward, with the ST chamber spiraling toward the manipulator magnet. Adjustments were made so that the manipulator rotation axis was approximately aligned with the central spiral axis of the cochlea.

The sensor itself experiences forces and torques from the manipulator magnet since the sensor is made of ferromagnetic material. Thus, to calibrate for these effects, insertion measurements were taken while running experiments without the CI prototype attached to the sensor. Five calibration runs were averaged and subtracted from the insertion measurements recorded with the prototype attached.

We conducted nonguided and magnetically guided experiments on the same CI, with all other factors held constant. During the experiments, the closest distance between the manipulator magnet and the CI tip corresponded to a dipole-to-dipole distance of 29 mm. The ideal trajectory for the prototype is one in which its tip avoids the most contact with the ST walls during the experiment. Toward this end, the position of the manipulator magnet (both rotation and translation toward the phantom) at each 1 mm discrete translation of the prototype was experimentally predetermined through visual inspection of the CI tip in relation to the ST walls (i.e., to maintain the tip parallel to the channel). With the maximum-field strategy, only the rotation of the manipulator magnet was predetermined. With the maximum-torque method, however, both parameters were predetermined with the additional constraint that the magnet dipoles were kept orthogonal to each other throughout the insertion. The predetermined manipulator trajectory was preprogrammed and automated with respect to the translation of the prototype. At each discrete 1 mm interval along this trajectory, 10 ms of force data were collected and averaged, until a total translation of 74 mm was achieved.

#### 4 Experimental Results

The measured insertion forces are shown in Fig. 9. The variance between runs was calculated and presented as solid vertical lines indicating the two-standard deviation interval at each depth. Insertion depths are measured from the initial implant position shown in Fig. 6. The vertical dashed lines show the approximate insertion depths where the implant first made contact with the phantom outer wall. Their corresponding images are shown in Fig. 9(d). For the nonguided insertions, initial outer-wall contact (which can be reasonably described as a direct impingement of the tip onto the wall) occurred at 17.5 mm. Using magnetic guidance, our prototype avoids contact with the first cochlear turn and clearly allows the CI to be inserted deeper into the ST phantom before it makes initial contact. Additionally, guided insertions produce a more distributed initial contact than nonguided insertions. For an

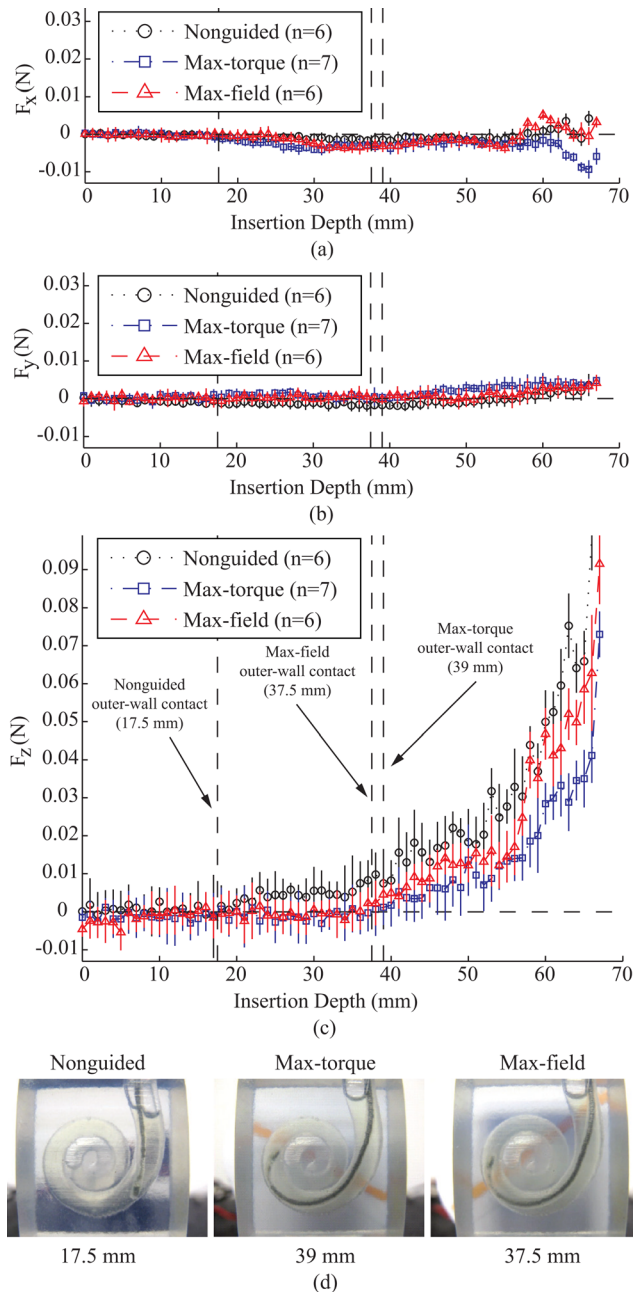


**Fig. 9** (a–c) Force measurements for all three insertion methods. The direction of  $F_x$ ,  $F_y$ , and  $F_z$  are defined in Fig. 4 and Fig. 6. Each data point represents the average of  $n$  runs, where the collected measurement for each run is an average of 10 samples at the corresponding insertion depth. The solid vertical bar with each data point shows the two-standard-deviation interval. Vertical dashed lines mark the approximate locations where the implant first made contact with the ST outer wall. (d) Corresponding images showing implant positions at first instance of outer-wall contact.

insertion depth between 0 mm and 25 mm, no method shows a clear advantage. However, the magnitudes of the forces in this region are so small that they are of limited interest. After 25 mm, the nonguided approach is inferior to both magnetically guided strategies. As long as the prototype avoids contact with the ST, insertions forces are negligible, and although the guided implant eventually slides against the ST outer wall, the CI touches the wall softer when using guidance, and the tip is bent away from the wall, decreasing both frictional and tip contact forces (Fig. 10). In general, nonguided insertions resulted in the highest force and the

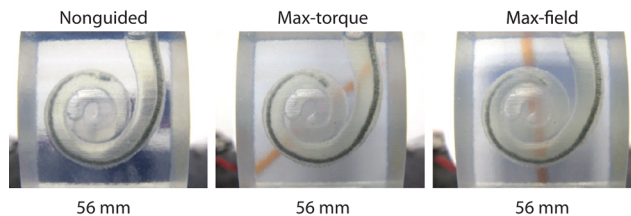


**Fig. 10** The tip of the implant is directed away from the outer wall using both the maximum-torque and maximum-field methods, even at significant insertion depths

maximum-torque method generally resulted in the lowest force. This is consistent with our hypothesized outcome described in Sec. 2: the maximum-torque method minimizes attractive forces between the CI and the manipulator magnet, which in turn minimizes lateral scraping on the ST wall. Nevertheless, any lateral scraping caused by attractive forces in the maximum-field method does not negate the benefits of guiding the CI tip through the channel. This is reasonable given that an estimate of the maximum attractive force of only 10 mN was computed using Eq. (7) at the closest dipole-to-dipole distance of 29 mm with the maximum-field method. These results show that insertion forces can be reduced by approximately 50% using magnetic guidance, indicating that significant insertion-force reduction is possible with our approach.

## 5 Discussion

Without guidance, the inherent stiffness in a free-fitting CI produces a mechanical restoring torque that presses the CI against the outer ST wall, resulting in increased friction and insertion force. With magnetic guidance, the torque acting on the CI tip counteracts this mechanical restoring torque. If the magnetic torque is sufficient, the CI will be directed completely away from the wall. If not, the magnetic torque will still provide some decrease in contact forces, as demonstrated by the reductions shown in Fig. 9. While the required applied torque is a function of the prototype's bending stiffness and its distribution, our main goal was not to determine the required torques needed to insert clinical CIs. Rather, this proof-of-concept study endeavored to demonstrate the viability of insertion-force reduction with the magnetic guidance strategies proposed. To this end, a rigorous method to measure the prototype's bending stiffness seemed unnecessary when a prototype that qualitatively matched the stiffness of a commercial CI was sufficient.

Our straight, free-fitting prototype limits the benefit of magnetic guidance since eventually the applied magnetic torque cannot overcome the natural tendency of the prototype to maintain its relaxed, straight shape. If the CI were fabricated so that its relaxed shape approximated the ST curvature (as is done with some current clinical CIs) then we could use our magnetic guidance concept to uncoil these precurled CIs during insertion and conceivably achieve near-zero insertion force throughout the insertion. An ideal prototype would exhibit the desired bending properties such that a magnetic torque applied at the tip results in the most desirable uncoiled shape for insertion. This type of design would also address the aforementioned, second widely accepted goal [1] in that close proximity between the CI and the modiolus reduces the power consumption required by the electrodes and the cross-talk responsible for poor frequency resolution due to one electrode stimulating multiple locations on the nerve.

A second way in which our prototype limits the benefit of magnetic guidance is that insertions into our ST phantom beyond 560 deg are precluded because our prototype's tip diameter (1.6 mm) exceeds the local channel height (1.41 mm). Unlike our prototype, which has a constant diameter throughout, real CIs have a tapered shape; that is, they are thicker at the base and thinner at the tip. Tapering future prototypes to have a smaller diameter

(and a smaller embedded magnet) would allow deeper insertion into the ST, and the tapered shape would help provide the necessary basal stiffness to avoid buckling.

To achieve better proximity to the modiolus, a class of pre-curved CIs have been developed that are initially straightened with an internal stylet (i.e., a stiff metal wire) but return to their original spiral shape after its removal. One of the more promising CIs in this class uses an insertion technique, known as advance-off-stylet (AOS), in which the electrodes are pushed off the stylet at the beginning of the first cochlear turn [1]. As reported by several groups [6–8], the AOS technique shows a notable decrease in forces for nearly the entire insertion procedure in part because this technique can eliminate contact between the CI and the outer wall of the first cochlear turn [1]. This is advantageous since most insertion trauma occurs at or near the first site of contact with the lateral wall of the ST (i.e., the first cochlear turn), and any additional trauma past this point seems minimal, mainly since low incidence angles between the CI and the lateral wall are no longer likely [20]. However, the CIs designed for this insertion technique are approximately 22 mm in length, which is very short compared to the longest free-fitting arrays currently available. As a result, deep insertions into the apical regions of the cochlea are not possible. Using magnetic guidance, our prototype similarly avoids contact with the first cochlear turn (Fig. 11), yet this concept can be applied to longer CIs to achieve deeper insertions. Additionally, our concept can be easily adapted to improve the advance-off-stylet insertion technique by straightening the CI during the critical moments when withdrawing the stylet can result in the CI curving into the ST inner wall (see Fig. 2(b)).

In the experiments herein, we used force sensing only for analysis after the insertion had been performed. Others have used force feedback to regulate insertion speed during their experiments using a steerable prototype electrode array [13]. It seems reasonable to utilize force measurements and control algorithms in real-time to minimize insertion forces adaptively throughout the insertion, essentially allowing the CI to “feel around in the dark,” as opposed to relying on medical imaging for guidance. This capability would be advantageous since preoperative imaging to determine the dimensions of the patient’s cochlea is not a current practice for CI surgery [1]. By including measured mechanical properties of the basilar membrane into a force control strategy, a surgeon can detect if the CI is about to rupture into adjacent cochlear chambers. Unexpected increases in force will be detected before they become problematic. Corrective action can be taken by adapting the guidance continuously or by reversing the insertion for a small distance and then modifying the magnetic guidance plan.

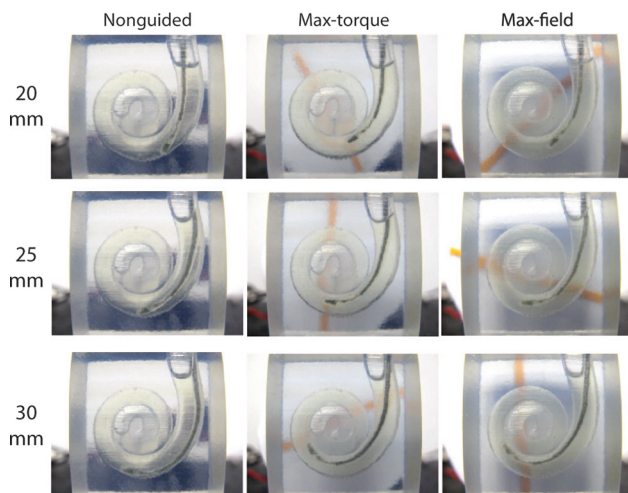


Fig. 11 Images of implant through the first turn

Implementing force feedback control is complicated by the fact that the force sensor is not collocated with the implant tip. Interpreting tip forces, especially since the implant is flexible, may be difficult. That is, forces on the tip (including ST contact forces and attractive magnetic forces) may not be easily measured with a force sensor located at the base. In the experiments of Fig. 9, the measured forces in the direction of the basilar membrane (y-direction of Fig. 4) did not exceed 2 mN even though the attractive magnetic force (as discussed earlier) is as high as 10 mN using the maximum-field strategy. That said, neither the estimated attractive force (10 mN) nor the measured force in the direction of the basilar membrane (2 mN distributed along the entire implant length) exceeded the force required to puncture the basilar membrane (26–35 mN as measured by one group [21]). Further, in our implementation, the dominant magnetic torque is used to align the implant tip in the direction of the ST channel, which is parallel to the ST walls (Fig. 10). Thus, the typical scenario of basilar perforation in which the electrode tip impinges on the basilar membrane is avoided. Clearly, the attractive forces on the implant did not increase the overall friction because the insertion force ( $F_z$ ) decreased with the use of magnetic guidance. This seems reasonable given that the friction due to lateral scraping from the attractive forces is partially muted by the soap solution. More importantly, the actual friction in a real insertion may only be about 1–2 mN (for the estimated 10 mN of attractive forces) based on measured friction coefficients (0.10–0.20) between clinical CIs and the endosteum lining of the ST [22]. Some attractive force may even be beneficial to direct the implant towards the apex of the cochlea (Fig. 3). This topic requires further investigation.

Our magnetic guidance approach can be scaled according to clinical demands. The magnetic field strength of any source is homothetic, meaning that the field of a permanent magnet is unchanged as the dimensions are scaled. The field gradient, however, is not homothetic. The field of a small magnet changes faster spatially than that of a large magnet. This can be demonstrated through some manipulation of Eqs. (5) and (6). If we scale the magnet’s linear dimensions by a factor  $s$  then its volume scales as  $s^3$ . Therefore, assuming identical magnetization, the dipole strength  $\mathbf{M}$  and the resulting field strength and gradient will also scale as  $s^3$ . Now suppose that we measure the field at a distance  $s|\mathbf{p}|$  from the scaled magnet so that the distance has been scaled by the same factor as the magnet’s linear dimensions. Equations (5) and (6) become

$$|\mathbf{B}| = \frac{\mu_0(s^3|\mathbf{M}|)}{4\pi(s^3|\mathbf{p}|^3)} = \frac{\mu_0|\mathbf{M}|}{4\pi|\mathbf{p}|^3} \quad (8)$$

and

$$\frac{d|\mathbf{B}|}{d|\mathbf{p}|} = -\frac{3\mu_0(s^3|\mathbf{M}|)}{4\pi(s^4|\mathbf{p}|^4)} = -\frac{3\mu_0|\mathbf{M}|}{4\pi|\mathbf{p}|^4} \left(\frac{1}{s}\right) \quad (9)$$

The field strength of a permanent magnet scaled by a factor  $s$  measured a scaled distance  $s|\mathbf{p}|$  away from the its center is the same as the field strength measured a distance  $|\mathbf{p}|$  away from the original magnet. This is the homothetic property of the field. The field gradient, however, is  $1/s$  times that of the originally measured gradient.

Our experimental setup and results used a scaled 3:1 implant prototype and ST phantom. The effects of scaling down to 1:1 can be initially assessed by modeling the implant as a cantilever beam with a pure torque at its tip, resulting in the following expression for the deflected angle at the tip [23]

$$\theta = \frac{TL}{EI} \quad (10)$$

where  $T$  is the torque applied at the implant tip,  $L$  and  $E$  are the length and Young’s modulus of the implant, respectively, and  $I$  is the moment of inertia of the cross-sectional area, which, if approximated as a circle of diameter  $d$ , is

$$I = \frac{\pi d^4}{64} \quad (11)$$

By substituting Eq. (11) into Eq. (10), the tip deflection angle can be expressed as

$$\theta = \frac{64TL}{\pi E d^4} \quad (12)$$

Scaling down the implant by a factor  $s$  will reduce the implant's length and diameter by the same factor  $s$ . To accommodate the smaller geometric constraints of the scaled-down implant, a smaller implant magnet will be required. If this is represented as a reduction in its linear dimension by the same factor  $s$ , then the volumetric reduction ( $s^3$ ) of the implant magnet reduces the applied torque at the tip by  $s^3$ . The result of scaling down the implant is no effect on the tip deflection angle, as seen in Eq. (13):

$$\theta = \frac{64(T/s^3)(L/s)}{\pi E (d/s)^4} = \frac{64TL}{\pi E d^4} \quad (13)$$

Scaling of the phantom does not affect the tip deflection angles required to navigate through it. Therefore, scaling our experiments down to 1:1 (i.e., reducing the implant, its magnet, and the phantom) likely will not have major effects on the results.

Having demonstrated scaling effects of the magnetic field and the implant, we can now discuss the approximate scale of a clinical arrangement. As indicated earlier, the nearest dipole-to-dipole distance in these experiments is about 30 mm. Increasing the dipole-to-dipole distance to 120 mm will require a 102-mm-diameter  $\times$  102-mm-long manipulator magnet to produce the same field strength as in our experiments. Since the distance from the apex of the cochlea to the edge of the head along the axis of the cochlea is approximately 60 mm, a 10 mm clearance between the edge of the head and the edge of the manipulator magnet can be achieved in a clinical setting with a 102-mm-diameter  $\times$  102-mm-long manipulator magnet. It should be noted that the manipulator magnet size can be reduced by increasing the grade of NdFeB magnet used, and the strength of the required field can be reduced by modifying certain implant design factors such as increased implant flexibility.

The effect of strong magnetic fields on implanted medical devices has been a longstanding concern ever since magnetic resonance (MR) scanners became a common diagnostic tool for clinicians. Numerous studies have scrutinized cochlear implants in the strong magnetic fields (1.5 T) of an MR scanner [24–26]. It is now generally accepted that heating and electrical stimulation in the electrodes of a cochlear implant electrode array due to eddy currents induced by changing magnetic fields in an MR scanner are largely negligible and well within healthy thresholds [26]. It also seems reasonable to expect that the electrode array does not shift during an MR scan since concerns over potential device displacement is typically associated with the internal receiver magnet [26] (see Fig. 1). Since the magnetic field in an MR scanner is significantly stronger than any field produced in our concept, it seems reasonable then to expect that any effect from the magnetic field (either from the manipulator or the implant magnet) on the actual electrodes in the cochlear implant electrode array is negligible.

Progress toward clinical feasibility will require several issues to be addressed. The obvious concerns regarding MR scanner safety can be addressed by a CI prototype design with a removable magnetic tip. Alignment of the manipulator rotation axis with the central axis of the cochlea may be difficult in practice and warrants some study on the effects of misalignment. Further, the implant magnet is never truly situated on the manipulator's axis of rotation (as shown in Fig. 4) since the implant magnet is always off-axis while tracing out the cochlear spiral. These off-axis effects warrant further study. In the conventional otologic position (Fig. 3), the initial insertion angle is not oriented as shown in our experiments. Improved *in vitro* studies should orient the phantom to

mimic the initial insertion angle and account for initial gravity effects on a flexible implant. Our experimental setup and results used a scaled 3:1 implant prototype and ST phantom. Eventually, these experiments must be performed at 1:1 scale, requiring a 1:1 scale implant and a 1:1 scale ST phantom with both cochleostomy and round-window openings and oriented to mimic the conventional otologic position. Deviations into other scalar chambers could not be assessed with our experiment since trajectories were preplanned through a phantom consisting of only the ST path. *In vitro* studies with ST phantoms and cadaver temporal bones directly comparing our prototype and insertion method against commercial CIs using standard techniques are required for proper evaluation.

## 6 Conclusion

We have presented a proof-of-concept study that demonstrates the efficacy of implementing magnetic guidance as a clinical strategy toward improved cochlear implant surgery. By applying magnetic torque to the tip of a cochlear-implant prototype during insertions, we reduced the insertions forces by approximately 50%. Such reductions will likely reduce insertion trauma by a proportional amount and may enable deeper insertion into the cochlea for improved performance.

## Acknowledgment

This work was supported by the National Science Foundation under Grants IIS-0952718 and DGE-0654414. This work appeared in part at the 2011 IEEE/RSJ International Conference on Intelligent Robots and Systems. This research is part of a larger collaboration with Dr. Robert Webster at Vanderbilt University, and the authors would like to thank him for fruitful discussions.

## References

- Rebscher, S. J., Hetherington, A., Bonham, B., Wardrop, P., Whinney, D., and Leake, P. A., 2008, "Considerations for Design of Future Cochlear Implant Electrode Arrays: Electrode Array Stiffness, Size, and Depth of Insertion," *J. Rehabil. Res. Dev.*, **45**(5), pp. 731–747.
- Briggs, R. J. S., Tykocinski, M., Saunders, E., Hellier, W., Dahm, M., Pyman, B., and Clark, G. M., 2001, "Surgical Implications of Perimodiolar Cochlear Implant Electrode Design: Avoiding Intracochlear Damage and Scala Vestibuli Insertion," *Cochlear Implants Int.*, **2**(2), pp. 135–149.
- Adunka, O., and Kiefer, J., 2006, "Impact of Electrode Insertion Depth on Intracochlear Trauma," *Otolaryngol. Head Neck Surg.*, **135**(3), pp. 374–382.
- Gstoettner, W., Franz, P., Hamzavi, J., Plenk, H., Baumgartner, W., and Czerny, C., 1999, "Intracochlear Position of Cochlear Implant Electrodes," *Acta Otolaryngol.*, **119**(2), pp. 229–233.
- Gstoettner, W. K., Adunka, O., Franz, P., Hamzavi, J., Plenk, H., Susani, M., Baumgartner, W., and Kiefer, J., 2001, "Perimodiolar Electrodes in Cochlear Implant Surgery," *Acta Otolaryngol.*, **121**(2), pp. 216–219.
- Roland, Jr., J. T., 2005, "A Model for Cochlear Implant Electrode Insertion and Force Evaluation: Results With a New Electrode Design and Insertion Technique," *Laryngoscope*, **115**(8), pp. 1325–1339.
- Todd, C. A., Naghdy, F., and Svehla, M. J., 2007, "Force Application During Cochlear Implant Insertion: An Analysis for Improvement of Surgeon Technique," *IEEE Trans. Biomed. Eng.*, **54**(7), pp. 1247–1255.
- Schurzig, D., Webster III, R. J., Dietrich, M. S., and Labadie, R. F., 2010, "Force of Cochlear Implant Electrode Insertion Performed by a Robotic Insertion Tool: Comparison of Traditional Versus Advance Off-Stylet Techniques," *Otol. Neurotol.*, **31**(8), pp. 1207–1210.
- Mirzadeh, H., and Abbasi, F., 2004, "Segmented Detachable Structure of Cochlear-Implant Electrodes for Close-Hugging Engagement with the Modiolus," *J. Biomed. Mater. Res. B Appl. Biomater.*, **68B**(2), pp. 191–198.
- Arcand, B. Y., Bhatti, P. T., Butala, N. V., Wang, J., Friedrich, C. R., and Wise, K. D., 2004, "Active Positioning Device for a Perimodiolar Cochlear Electrode Array," *Microsys.Tech.*, **10**(6), pp. 478–483.
- Wu, J., Yan, L., Xu, H., Tang, W. C., and Zeng, F.-G., 2005, "A Curvature-Controlled 3D Micro-Electrode Array for Cochlear Implants," IEEE 13th International Conference on Solid-State Sensors, Actuators and Microsystems, TRANSDUCERS '05, Vol. 2, Seoul, Korea, June 5–9, pp. 1636–1639.
- Chen, B., Kha, H. N., and Clark, G. M., 2007, "Development of a Steerable Cochlear Implant Electrode Array," 3rd Kuala Lumpur International Conference on Biomedical Engineering 2006 (*IFMBE Proceedings*), Vol. 15 pp. 607–610.

- [13] Zhang, J., Roland, Jr., J. T., Manolidis, S., and Simaan, N., 2009, "Optimal Path Planning for Robotic Insertion of Steerable Electrode Arrays in Cochlear Implant Surgery," *ASME J. Med. Devices*, **3**(1), p. 011001.
- [14] Zhang, J., Wei, W., Ding, J., Roland, Jr., J. T., Manolidis, S., and Simaan, N., 2010, "Inroads Toward Robot-Assisted Cochlear Implant Surgery Using Steerable Electrode Arrays," *Otol. Neurotol.*, **31**(8), pp. 1199–1206.
- [15] Majdani, O., Schurzig, D., Hussong, A., Rau, T., Wittkopf, J., Lenarz, T., and Labadie, R. F., 2010, "Force Measurement of Insertion of Cochlear Implant Electrode Arrays in Vitro: Comparison of Surgeon to Automated Insertion Tool," *Acta Otolaryngol.*, **130**(1), pp. 31–36.
- [16] Schurzig, D., Labadie, R. F., Hussong, A., Rau, T. S., and Webster III, R. J., 2012, "Design of a Tool Integrating Force Sensing With Automated Insertion in Cochlear Implantation," *IEEE/ASME Trans. Mechatronics*, **17**(2), pp. 381–389.
- [17] Clark, J. R., Warren, F. M., and Abbott, J. J., 2011, "A Scalable Model for Human Scala-Tympani Phantoms," *ASME J. Med. Devices*, **5**(1), p. 014501.
- [18] Maghribi, M. N., Krulevitch, P. A., Davidson, J. C., and Hamilton, J. K., 2006, "Implantable Devices Using Magnetic Guidance," U.S. Patent No. 0052656.
- [19] Abbott, J. J., Ergeneman, O., Kummer, M. P., Hirt, A. M., and Nelson, B. J., 2007, "Modeling Magnetic Torque and Force for Controlled Manipulation of Soft-Magnetic Bodies," *IEEE Trans. Robot.*, **23**(6), pp. 1247–1252.
- [20] Zeng, F.-G., Rebscher, S., Harrison, W., Sun, X., and Feng, H., 2008, "Cochlear Implants: System Design, Integration, and Evaluation," *IEEE Rev. Biomed. Eng.*, **1**, pp. 115–142.
- [21] Ishii, T., Takayama, M., and Takahashi, Y., 1995, "Mechanical Properties of Human Round Window, Basilar and Reissner's Membranes," *Acta Otolaryngol.*, **115**(s519), pp. 78–82.
- [22] Kha, H. N., and Chen, B. K., 2006, "Determination of Frictional Conditions Between Electrode Array and Endosteum Lining for Use in Cochlear Implant Models," *J. Biomech.*, **39**(9), pp. 1752–1756.
- [23] Howell, L. L., 2001, *Compliant Mechanisms*, John Wiley & Sons, Inc., New York.
- [24] Teissl, C., Kremser, C., Hochmair, E. S., and Hochmair-Desoyer, I. J., 1999, "Magnetic Resonance Imaging and Cochlear Implants: Compatibility and Safety Aspects," *J. Magn. Reson. Imaging*, **9**(1), pp. 26–38.
- [25] Gubbels, S. P., and McMenomey, S. O., 2006, "Safety Study of the Cochlear Nucleus 24 Device With Internal Magnet in the 1.5 Tesla Magnetic Resonance Imaging Scanner," *Laryngoscope*, **116**(6), pp. 865–871.
- [26] Crane, B. T., Gottschalk, B., Kraut, M., Aygun, N., and Niparko, J. K., 2010, "Magnetic Resonance Imaging at 1.5 T After Cochlear Implantation," *Otol. Neurotol.*, **31**(8), pp. 1215–1220.